University of Nebraska - Lincoln
DigitalCommons@University of Nebraska - Lincoln

US Department of Energy Publications | US Department of Energy

1-1-2003

Mossbauer and optical spectroscopic study of temperature and redox effects on iron local environments in a Fe-doped (0.5 mol% Fe2O3)18Na2O–72SiO2 glass

Ravi K. Kukkadapu
Pacific Northwest National Laboratory, ravi.kukkadapu@pnl.gov

Hong Li
Pacific Northwest National Laboratory

Gary L. Smith
Pacific Northwest National Laboratory

J.D. Crum
Pacific Northwest National Laboratory

Jun-Sik Jeoung
University of Arizona- Tucson

See next page for additional authors

Follow this and additional works at: http://digitalcommons.unl.edu/usdoepub

Part of the Bioresource and Agricultural Engineering Commons

Kukkadapu, Ravi K.; Li, Hong; Smith, Gary L.; Crum, J.D.; Jeoung, Jun-Sik; Poisl, W. Howard; and Weinberg, Michael C., "Mossbauer and optical spectroscopic study of temperature and redox effects on iron local environments in a Fe-doped (0.5 mol% Fe2O3)18Na2O–72SiO2 glass" (2003). *US Department of Energy Publications.* Paper 168.
http://digitalcommons.unl.edu/usdoepub/168

This Article is brought to you for free and open access by the US Department of Energy at DigitalCommons@University of Nebraska - Lincoln. It has been accepted for inclusion in US Department of Energy Publications by an authorized administrator of DigitalCommons@University of Nebraska - Lincoln.

Authors
Ravi K. Kukkadapu, Hong Li, Gary L. Smith, J.D. Crum, Jun-Sik Jeoung, W. Howard Poisl, and Michael C. Weinberg

This article is available at DigitalCommons@University of Nebraska - Lincoln: http://digitalcommons.unl.edu/usdoepub/168

Available online at www.sciencedirect.com
SCIENCE DIRECT®
Journal of Non-Crystalline Solids 317 (2003) 301–318
JOURNAL OF NON-CRYSTALLINE SOLIDS
www.elsevier.com/locate/jnoncrysol

Mössbauer and optical spectroscopic study of temperature and redox effects on iron local environments in a Fe-doped (0.5 mol% Fe_2O_3) $18Na_2O$–$72SiO_2$ glass

Ravi K. Kukkadapu [a,b,*], Hong Li [b,1], Gary L. Smith [b], J.D. Crum [b], Jun-Sik Jeoung [c], W. Howard Poisl [c], Michael C. Weinberg [c]

[a] *Environmental Molecular Science Laboratory, Richland, WA 99352, USA*
[b] *Pacific Northwest National Laboratory, Richland, WA 99352, USA*
[c] *Department of Materials Science and Engineering, The University of Arizona, Tucson, AZ 85721, USA*

Received 18 March 2002

Abstract

Local environments of ferric and ferrous irons were systematically studied with Mössbauer (at liquid helium temperature) and ultraviolet–visible–near infrared spectroscopic methods for various $18Na_2O$–$72SiO_2$ glasses doped with 0.5 mol% Fe_2O_3. These were prepared at temperatures of 1300–1600 °C in ambient air or at 1500 °C under reducing conditions with oxygen partial pressures from 12.3 to 0.27×10^{-7} atmospheres. The Mössbauer spectroscopic method identified three types of local environments, which were represented by the Fe^{3+} sextet, the Fe^{3+} doublet, and the Fe^{2+} doublet. The Fe^{3+} sextet ions were assigned to 'isolated' octahedral ions. Under reducing conditions, the octahedral Fe^{3+} ions were readily converted into octahedral ferrous ions. The Fe^{3+} doublet exists both in octahedral and tetrahedral environment, mainly as tetrahedral sites in the reduced samples. The tetrahedral ions were found stable against reduction to ferrous ions. The Fe^{2+} doublet sites existed in octahedral coordination. Combining results from both spectroscopic studies, the 1120- and 2020-nm optical bands were assigned to octahedral ferrous ions with a different degree of distortion rather than different coordinations. Further, we assigned the 375-nm band to the transition of octahedral ferric ions that are sensitive to the change of oxygen partial pressure in glass melting and 415-, 435-, and 485-nm bands to the transitions of the tetrahedral ferric ions that are insensitive to oxidation states of the melt. The effect of ferric and ferrous ions with different coordination environments on the glass immiscibility was elucidated.
© 2002 Elsevier Science B.V. All rights reserved.

1. Introduction

Iron derived from nuclear fuel reprocessing is one of the major components in high-level radioactive waste (HLW) glasses. In the United States, HLW glasses are primarily based on borosilicate systems [1–3]. Iron in HLW glasses exits

* Corresponding author. Tel.: +1-509 376 3795; fax: +1-509 376 3650.
E-mail address: ravi.kukkadapu@pnl.gov (R.K. Kukkadapu).
[1] Present address: Fiber Glass Science and Technology, Glass Technology Center, PPG Industries Inc., Pittsburgh, PA 15230, USA.

0022-3093/03/$ - see front matter © 2002 Elsevier Science B.V. All rights reserved.
PII: S0022-3093(02)01815-X

This article is a U.S. government work, and is not subject to copyright in the United States.

both in ferrous and ferric forms, their ratio being affected by host glass composition as well as processing temperature and oxygen partial pressure [4–7]. There are at least two major related issues with iron in HLW glasses: vitrification processing and waste-form performance. The processing issue is related to the formation of spinel crystal, a solid solution of iron oxide with other minor species from waste streams, such as Ni, Cr, and Mn [8–12]. Spinel crystal settling and accumulation at the bottom of a HLW vitrification melter or in a glass pour spot is detrimental. Studies of spinel-crystallization issues in the waste glasses have been reported and used to aid in developing waste-glass formulations that are not susceptible to spinel formation, i.e., low liquidus temperature for spinel as a primary phase [13,14]. The performance issue related to iron is how ferrous and ferric iron or iron redox affects the tendency of the HLW glass stability, i.e., whether a change in iron redox of glass influences the tendency of glass phase separation since waste glass poured into a canister will be subject to both slow cooling and repeated heating during filling. Microphase separation can adversely impact the chemical durability of the final waste form [15,16]. The phase-separation study related to iron, specifically the iron redox, is limited [17,18]. For both processing and performance issues, a basic understanding of iron chemistry in the waste glasses is very important to ensure that the HLW glass formulation is optimized for both a safe vitrification process and the long-term stability of the final waste form under a radiation field and a geological environment.

On the one hand, borosilicate glasses can be generally viewed as a continuous network through linkages of the network formers of SiO_2 and B_2O_3 groups. On the other hand, numerous spectroscopic studies show that a borosilicate glass system may be more appropriately treated as a mixture of borate-rich and silicate-rich environments [19–23]. It follows that a random mixing between B–O and Si–O does not likely exist at a sub-nanoscale. Therefore, understanding ferrous and ferric iron effects on the phase stability of each individual glass-forming network, silicate versus borate, is important. This study investigated the effect of iron redox on the phase stability of silicate glass.

Sodium-silicate glasses, $13Na_2O$–$87SiO_2$ (13NS) and $18.56Na_2O$–$71.44SiO_2$ (18NS) are prone to microphase separation [18]. The effect of iron redox, $Fe^{2+}/(Fe^{2+} + Fe^{3+})$ or $\chi_{Fe(II)}$, on the critical temperature (T_c) of the two silicate glasses has been reported [18]. With 0.5 mol% Fe_2O_3 doping in the 13NS and 18NS glasses, there was an initial T_c downshift of −32 and −29 °C for the iron-doped 13NS with $\chi_{Fe(II)} = 0.097$ and 18NS glass with $\chi_{Fe(II)} = 0.058$, respectively, for the two glasses prepared under ambient conditions. Under reducing conditions, T_c slightly increased over the range of $\chi_{Fe(II)}$ from 0.097 to 0.66 for 13NS and from 0.058 to 0.89 for 18NS, respectively. The finding on the effect of iron redox on silicate phase separation is not well understood. To gain a better understanding of the observed iron redox effect, iron-doped 18NS glasses that were prepared under different oxidizing/reducing conditions were chosen for further study using Mössbauer and ultraviolet–visible–near infrared (UV–VIS–NIR) methods.

2. Experimental

2.1. Glass preparation

The baseline glass, $18.56Na_2O$–$71.44SiO_2$ (as analyzed composition), referred to as an 18NS glass in this study, was obtained from Owens–Corning, and it was homogenized at 1600 °C for five days. Fe-doped glasses were prepared by doping 0.5 mol% Fe_2O_3 in the glass and melting under different conditions: (1) in air with different temperatures, 1300, 1400, 1500, and 1600 °C and (2) at 1500 °C under different oxygen partial pressures by bubbling a mixture of CO and CO_2 gas in each melt. The gas mixing ratios of CO over CO_2 was 12/88, 24/76, 36/64, and 50/50, respectively, which correspond to oxygen partial pressures of 12.3, 2.3, 0.72, and 0.27×10^{-7} atmospheres, respectively, as calculated using a commercial software FACT [24]. The details of the iron-bearing glass preparation were previously discussed [18].

2.2. UV–VIS–NIR spectroscopy

A UV–VIS–NIR spectrophotometer was used to measure optical absorption spectra of the glass plates. The glass was cut into pieces with dimensions of 10×10 mm with varying thickness (1.5, 2.0, 2.5 and 3.0 mm) using a low-speed diamond saw. All of the glass samples were then ground using flat alumina grinding media and polished using 1-μm CeO_2 grit to achieve uniform thickness and parallel and polished surfaces. We calculated the extinction coefficient using the Lambert–Beer equation. To find the extinction coefficient, the concentration of $\chi_{Fe(II)}$ obtained from the colorimetric method was used as reported elsewhere [18]. Spectra were measured over the 200–3200 nm wavelength range with a 0.2-nm scan interval and a 0.1 s dwell time. The spectra were normalized by the sample thickness and corrected for background. The background correction was done by subtracting the spectrum of the baseline glass without iron from the spectrum of the iron-bearing glass.

2.3. Mössbauer spectroscopy

Samples (or absorbers) were prepared by mixing approximately 180 mg of powdered glass sample with petroleum jelly in a Cu holder (0.5 in. thick and 0.5 in. i.d.) that was sealed at one end with clear scotch tape. The sample space volume was filled with petroleum jelly and the ends sealed with a tape and an aluminized-Mylar film stable at 4.2 K. Because of the low absorber densities, thickness corrections were not applied. Liquid helium measurements were performed using a top-loading Janis exchange-gas cryostat. The temperature was continuously monitored with a Nichrome thermocouple. The temperature of the chamber was maintained within ±0.5 K with a temperature controller. The entire drive-source assembly was external to the cryostat, and only the sample was cooled to the desired temperature.

Spectra were collected using a ^{57}Co/Rh single-line thin source with an initial activity of 50 mCi. The Mössbauer bench (MB-500; WissEL, Germany) was equipped with a dual Mössbauer drive system to gather data simultaneously for two experiments. The velocity transducer (MVT-1000; WissEL) was operated in the constant-acceleration mode (23 Hz, ±10 or ±15 mm/s). Data were acquired on 1024 channels and then folded with a recoil (University of Ottawa) program to 512 channels to give a flat background and a zero-velocity position corresponding to the center shift (CS or δ) of a metallic-Fe foil at room temperature (RT). Calibration spectra were obtained with a 20-μm-thick α-Fe foil (Amersham, England) placed in exactly the same position as the samples to minimize any error due to changes in geometry. The transmitted radiations were recorded with Ar–Kr proportional counters. The spectra were evaluated with a recoil program using the Voigt-based hyperfine parameter distribution method of Rancourt and Ping [25].

2.4. Voigt-based hyperfine distribution method

Quantum mechanics predicts a Lorentzian shape for an emission (or absorption) line when a quantum emitter (or absorber) is involved [26]. The full width at half maximum Γ of the peak is a property of the particular nuclear transition and is expressed by the Heisenberg uncertainty relation, $\Gamma = \hbar/\tau$ ($\hbar$ is the Planck's constant divided by 2π, and τ is the exponential lifetime of the excited state). In ^{57}Fe Mössbauer spectroscopy, the 14.4-keV state has $\tau = 141$ ns and $\Gamma = 4.66 \times 10^{-9}$ eV (or 0.097 mm/s). For an absorption experiment, the predicted Γ is 0.194 mm/s (2×0.097 mm/s). The Γ value is not an adjustable parameter and hence was fixed at 0.194 mm/s for simulating the spectra of thin absorbers as used in this study. In the literature, however, it has become a widespread practice to employ an arbitrary number of Lorentzian doublets/sextets with adjustable Γ values. Such a fitting approach would carry a risk of over-interpretation of the physical meaning of the fitted Γ-value, which has been adequately addressed by Rancourt [27].

In the present work, the Voigt-based hyperfine distribution method developed by Rancourt and Ping [25], in which all the parameters have direct physical meanings, was employed. In addition, FWHM was fixed at 0.194 mm/s in all the spectral simulations. The adopted fitting methodology

based on the hyperfine distribution method was found more physical and robust. Rancourt and Rancourt et al. [28,29] have recently discussed and illustrated the inadequacy of Lorentzian peaks in fitting mica spectra. The QSD distribution method assumes a certain number of generalized Fe environments (sites), each having its own continuous distribution of quadrupole splitting (Δ or QS) or hyperfine magnetic field (B_{hf}) that consists of a number of Gaussian components. The CS (δ) of each QSD site is related to its Δ, as $\delta = \delta_0 + \delta_1\Delta$, where δ_0 is the value of δ when Δ (a distribution rather than a singular value) is zero, and δ_1 is the coupling of δ to the distributed hyperfine parameter (Δ). For the hyperfine field distribution (HFD) site, the δ is related to its Zeeman splitting, z, as $\delta = \delta_0 + \delta_1 z$. Rossano et al. [30] recently applied two-dimensional distributions of δ and Δ to explain the nature of Fe^{2+} sites in tektite glasses. In the present study, δ_1 was fixed at zero in all the simulations, which is often a valid assumption since local structural and chemical variations have a much smaller effect on δ than on Δ. The quadrupole shift parameter, ε, of the HFD site is related to its z, as $\varepsilon = \varepsilon_0 + \varepsilon_1 z$, where ε_0 is the value of ε when z (a distribution) is zero, and ε_1 is the coupling of ε to the distributed hyperfine parameter. Again ε_1 was fixed at zero in all the simulations.

3. Results

3.1. UV–VIS–NIR

The UV–VIS–NIR spectra of the glasses melted at various temperatures (1300–1600 °C) and the glasses melted at 1500 °C under varying reducing conditions (CO/CO_2 ratio varying from 12/88 to 50/50) are shown in Fig. 1. All the glasses, regardless of the melting conditions, exhibited (1) broad peaks with maxima centered near 1120 and 2020 nm (Fig. 1(a), (b), (d), and (e)) and (2) minor

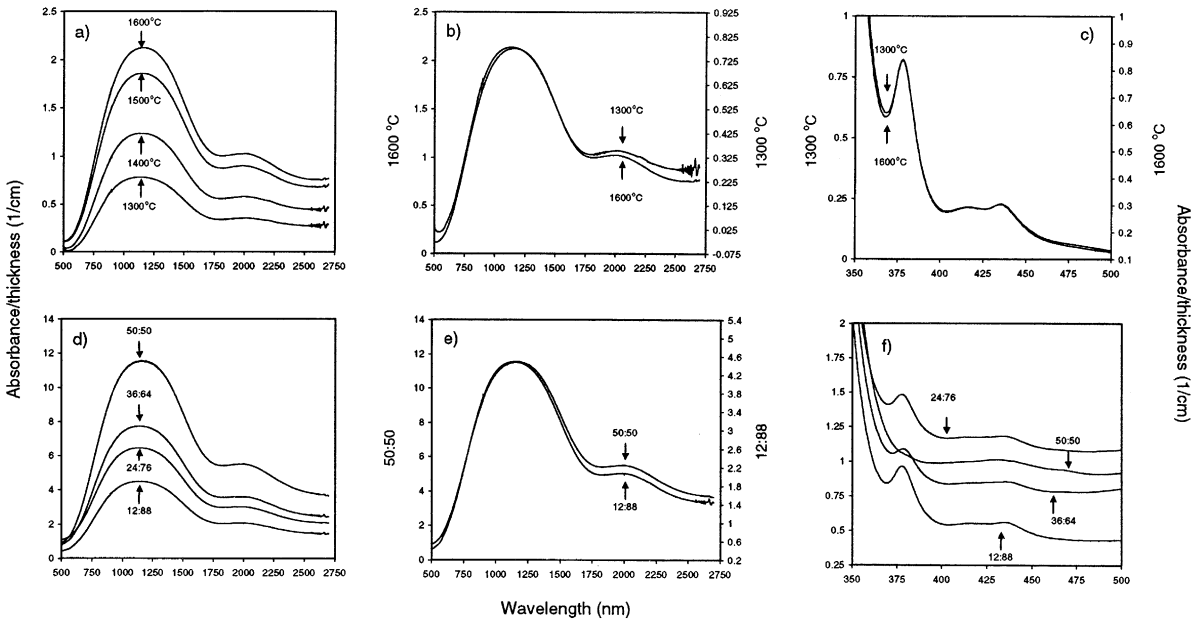

Fig. 1. UV–VIS–NIR spectra: (a) temperature effects on 1120- and 2020-nm band intensities for glasses melted between 1300 and 1600 °C in air, (b) little independent temperature effect on 1120- and 2020-nm band intensities for glasses melted between 1300 and 1600 °C (with two extreme cases), (c) no effect on UV absorption bands (with two extreme cases), (d) oxygen partial pressure effect on the 1120- and 2020-nm band intensities for the reduced glasses melted at 1500 °C under 12.3 ($12CO/88CO_2$) to 0.27×10^{-7} ($50CO/50CO_2$) atmosphere, (e) little independent temperature effect on 1120- and 2020-nm band intensities for the reduced glasses (with two extreme cases), (f) oxygen partial pressure effect on UV bands for the reduced glasses.

peaks centered around 375, 415, and 435 nm, and a broad peak at approximately 485 nm (Fig. 1(c) and (f)). The broad peaks centered near 1120 and 2020 nm are typical of the Fe^{2+} transition whereas the minor peaks at 375, 415, and 435 as well as the broad peak centered near 485 nm are characteristic of Fe^{3+} transitions [31].

The intensities of both the 1120- and 2020-nm bands due to Fe^{2+} were progressively higher in the samples melted in air at higher temperatures (Fig. 1(a)). However, the intensity ratio of the 1120-nm peak over the 2020-nm peak remained more or less constant for all the samples; as an example, spectra of 1300 and 1600 °C (lowest and highest temperature melted samples) are shown in Fig. 1(b) where the spectra were compared by plotting with different *y*-axes. Furthermore, it appears that the minor bands near 375, 415, and 435 nm as well as 485 nm due to Fe^{3+} bands were identical to each other in all the air-melted samples. As an example, spectra of 1300 and 1600 °C were compared in Fig. 1(c).

The Fe^{2+} bands of the reduced samples were qualitatively similar in shape and position to those of the samples made under ambient conditions, yet their intensities were much higher than those in Fig. 1(a). The intensities of the Fe^{2+} bands were progressively higher in the samples melted at lower oxygen partial pressures (Fig. 1(d)). However, similar to the finding for the samples prepared under ambient conditions, the intensity ratio of the 1120-nm band over the 2020-nm band changed a little. This observation was based on Fig. 1(e) where samples reduced at the highest and lowest oxygen partial pressures (12/88 and 50/50 $CO:CO_2$ atmosphere) were compared. On the other hand, unlike in the samples prepared in ambient conditions, there were significant changes in the intensities of the Fe^{3+} bands at lower wavelengths as shown in Fig. 1(f). For example, in the glass melted under the $36CO/64CO_2$ reducing condition, the band at 375 nm was shifted towards a higher wavelength as compared to that of the glasses melted under the $12CO/88CO_2$ and $24CO/76CO_2$ conditions. Most significant change, however, was absence of 375-nm band in the glass melted under the $50CO/50CO_2$ reducing condition. While changes occurred in the 375-nm peak in the reduced sample, there appeared little change in the 415-, 435-, and 485-nm bands.

3.2. Mössbauer

A curved baseline was evident in spectra of all the samples melted in air or under reducing conditions except for under highly reduced conditions, $36CO/64CO_2$ and $50CO/50CO_2$, respectively. The spectra were complex. Room and liquid helium (4.2 K) temperature spectra of the sample melted in air at 1600 °C are shown in Fig. 2 as an example. The RT spectrum was principally an asymmetric doublet suggesting overlapping between Fe^{2+} and Fe^{3+} doublet spectra with a curved baseline. The peak near 2 mm/s (marked with (∗) in Fig. 2) is typical of an Fe^{2+} doublet's high-energy component [32], whereas the broad feature over the 0–1 mm/s region is typical of a mixture of peaks (marked with (∗∗) in Fig. 2) for the Fe^{3+} doublet peaks and the Fe^{2+} doublet's low-energy component [32]. The curved baseline indicated the presence of 'isolated' Fe^{3+} sites that give rise to sextets at lower temperatures as clearly illustrated by the 4.2 K spectrum for the same sample. Such a phenomenon has been also reported in glasses with less than 4 wt% Fe_2O_3 [33–35], and kaolinite (an aluminosilicate clay) containing less than 1 wt% Fe [36]. The sextets, which make up about 75% of the

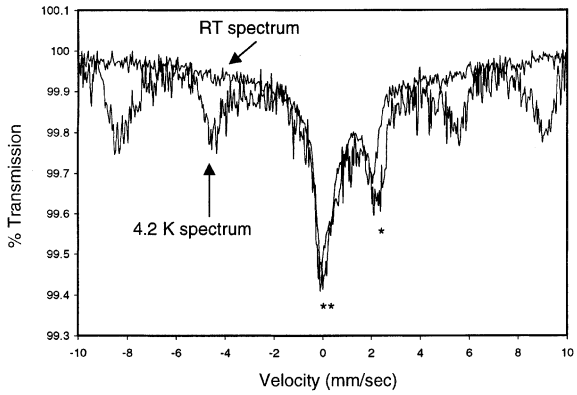

Fig. 2. RT and helium temperature 4.2 K ^{57}Fe Mössbauer spectra of the glass melted at 1600 °C in air showing an advantage, revealing presence of Fe^{3+} sextet, of conducting the test at 4.2 K.

spectral area, are usually referred to as hyperfine split (HFS) spectra.

The air-melted samples, however, differed mainly from each other in their central asymmetric double profile. The baseline and Fe^{3+} sextet features, on the other hand, appeared similar to each other. The 4.2 K Mössbauer spectra of the samples melted in air at 1300 and

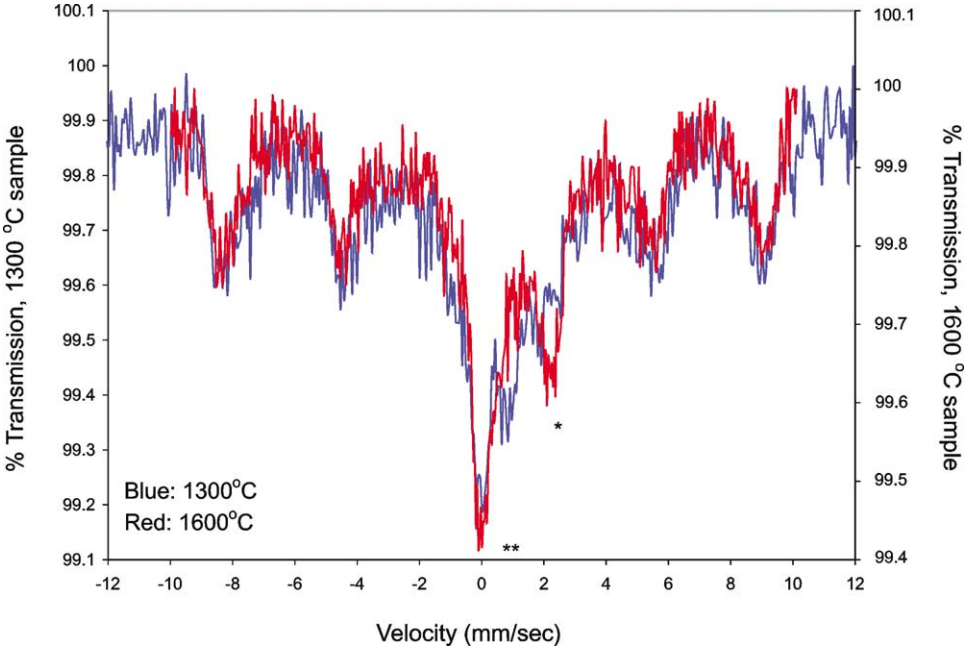

Fig. 3. ^{57}Fe Mössbauer spectra of glasses melted at 1300 (blue) and 1600 °C (red) in air.

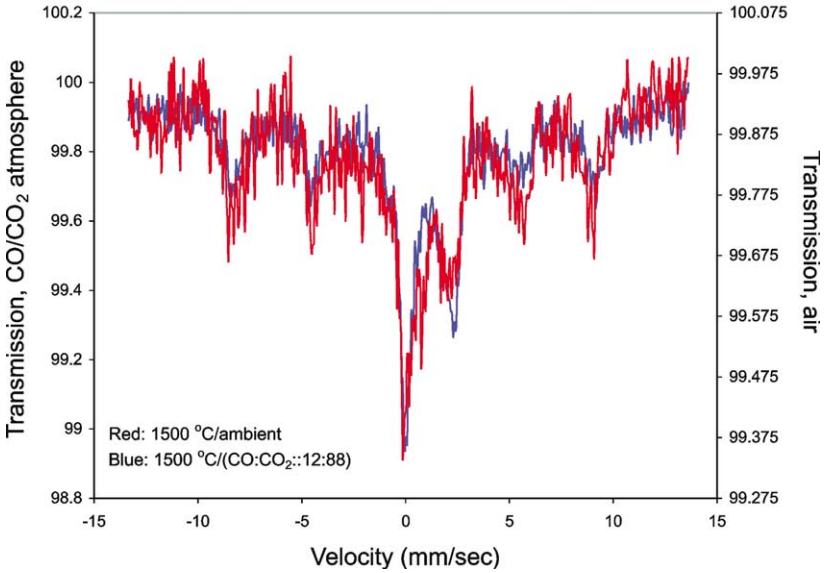

Fig. 4. ^{57}Fe Mössbauer spectra of glasses melted at 1500 °C in air (red) and under $12CO/88CO_2$ reducing atmosphere (blue).

1600 °C (lowest and highest melted samples) are shown in Fig. 3 as an example. From the figure, it is clear that the intensity of the Fe^{2+} doublet's high-energy component (marked with (∗) in Fig. 3) was relatively higher while the intensity of the Fe^{3+} doublet's low-energy component (marked with (∗∗) in Fig. 3) was relatively lower in the 1600 °C sample compared to the components in the 1300 °C sample. The relative intensities of the Fe^{2+} and Fe^{3+} doublet peaks in the intermediate sample, 1500 °C (Fig. 4), as expected, was in between the 1300 and 1600 °C samples.

The spectra of samples melted under the CO/CO_2 atmosphere were significantly different from those melted under ambient temperature. This observation was based on Fig. 4 where 4.2 K spectra of samples melted at 1500 °C in air and $12CO/88CO_2$ were compared. The intensity of the Fe^{2+} doublet's high-energy component was significantly higher in the sample melted in the presence of the $12CO/88CO_2$ atmosphere than in the air-melted sample. In addition, the comparison suggested that the CO/CO_2 atmosphere did not significantly affect the baseline and sextet feature (Fig. 4). Fig. 5 shows 4.2 K spectra of all the CO/CO_2 reduced glasses. The $12CO/88CO_2$ and $24CO/76CO_2$ reduced samples appeared to be different from each other, mainly in the asymmetric doublet profile; a closer inspection, however, also suggested a decrease in the curvature of the baseline feature. The $36CO/64CO_2$-reduced sample, on the other hand, was significantly different from the $12CO/88CO_2$ and $24CO/76CO_2$ reduced samples, and this was apparent from (1) a shift in the Fe^{2+} doublet's high-energy component towards higher energy, (2) an increase in the Fe^{3+} sextet's B_{hf} (splitting between the peaks 1 and 6; (∗) in the figure), (3) a decrease in the Fe^{3+} sextet's relative intensity, and (4) flattening of the baseline. On the other hand, the asymmetric doublet profile, mainly in terms of splitting between the doublet peaks, of the sample reduced under the highest CO/CO_2 ratio gas atmosphere, $50CO/50CO_2$, appears to be qualitatively similar to the $12CO/88CO_2$ and $24CO/76CO_2$ reduced sample profiles. Finally, the Fe^{3+} sextet feature was undetectable in the highly reduced sample.

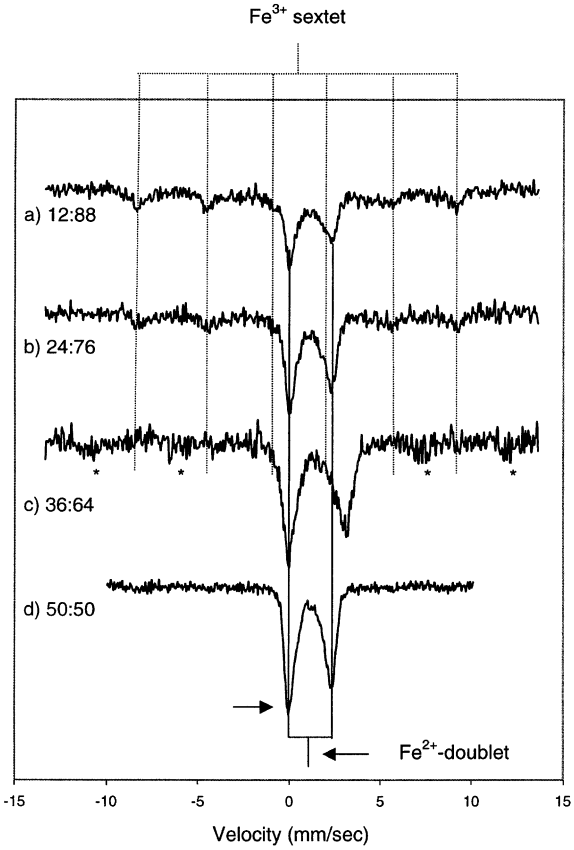

Fig. 5. ^{57}Fe Mössbauer spectra of glasses melted at 1500 °C in air under reducing atmospheres of (a) $12CO/88CO_2$, (b) $24CO/76CO_2$, (c) $36CO/64CO_2$, and (d) $50CO/50CO_2$.

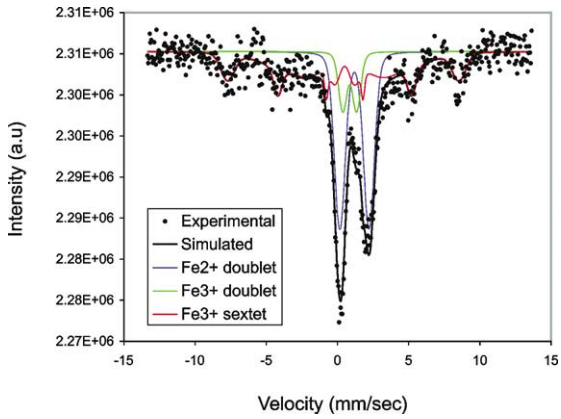

Fig. 6. Simulation of local iron environments based on 4.2 K ^{57}Fe Mössbauer spectrum of the NIST standard obsidian rock.

3.3. Mössbauer spectroscopy simulations

The quadrupole/hyperfine distribution method was adopted, as discussed earlier, to fit the spectra. Since the sextet feature of the samples was evident only at liquid helium temperature, simulations were carried out on 4.2 K spectra only. In the simulations, the spectra were fitted with three Fe sites, namely, an Fe^{3+} doublet, an Fe^{3+} sextet, and an Fe^{2+} doublet (see Figs. 6 and 7). In addition, for the samples that exhibited a curved baseline, we imposed a bimodal distribution (two Gaussian components) to fit the Fe^{3+} sextet. This approach yielded fitted parameters with better physical meaning. Furthermore, the fitting derived $\chi_{Fe(II)}$ ($\chi_{Fe(II)} = Fe^{2+}/\sum Fe$; $\sum Fe = Fe^{2+}_{(doublet)} + Fe^{3+}_{(doublet)} + Fe^{3+}_{(sextet)}$) values, assuming identical *f*-factors (recoil-free factor) for all the Fe environ-

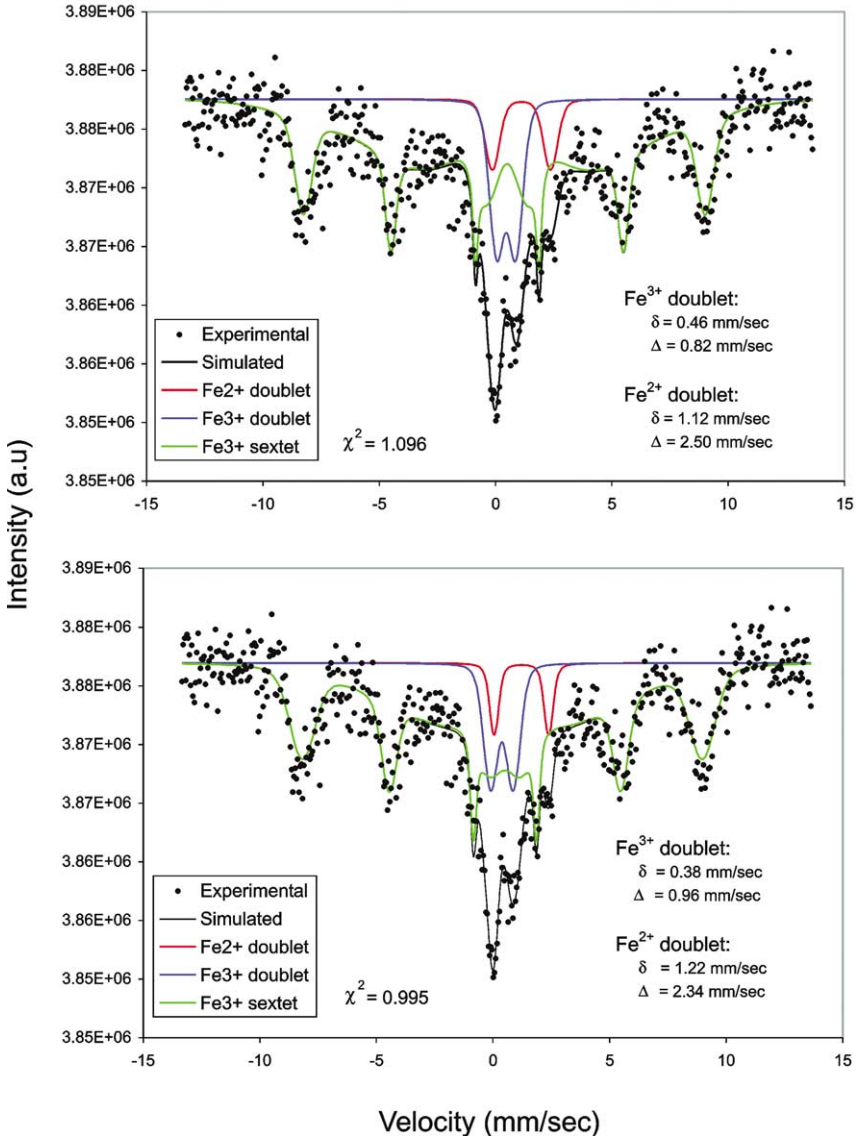

Fig. 7. Model simulation comparison based on 4.2 K ^{57}Fe Mössbauer spectrum of the glasses melted at 1300 °C in air.

ments, had a closer agreement with the $\chi_{Fe(II)}$ values determined by the spectrophotometric method [18]. The robustness of the simulation method adopted in this study was further demonstrated by fitting the 4.2 K spectrum for a standard obsidian rock (1.058% Fe^{2+} and 1.428% Fe^{3+}) from the National Institute for Standards and Testing (NIST) as shown in Fig. 6. Our fitting-derived $\chi_{Fe(II)}$ value was 0.428 ± 0.012 compared to the NIST certified value of 0.426.

On the other hand, as in other fitting methods such as the Lorentzian-based fit methods, there was always a concern of not extracting accurate Mössbauer parameters (e.g., δ and Δ) and spectral areas due to trade-off of parameters (and areas) between the different Fe-sites. For example, Fig. 7 shows statistically equivalent fits of the 1300 °C sample with different δ, Δ, and $\chi_{Fe(II)}$ values. The range in Δ values, particularly for the Fe^{3+} doublet, makes it difficult to comment on its coordination. Thus, it was difficult to approve or disapprove the simulation-derived Fe local environments from the Mössbauer study of a single sample. However, reasonably good fits that are physical can be obtained by drawing comparisons between the samples by monitoring the evolution or disappearance of peaks and changes in apparent Mössbauer parameters of various peaks. This approach coupled with supporting evidence from other analytical/spectroscopic data usually strengthens the quality of a fit of the data. For example, in the present study, a fit that exhibits realistic Mössbauer parameters and yields a $\chi_{Fe(II)}$ value close to the value derived by the UV–VIS–NIR technique was considered a good and meaningful fit.

3.3.1. Samples prepared in ambient air at different temperatures

The Mössbauer fitting parameters and the iron redox values or $\chi_{Fe(II)}$ for the glasses melted at three different temperatures, 1300, 1500, and 1600 °C, are summarized in Table 1. [2] The fit parameters are defined as follows: δ or CS is the center shift, Δ or QS is the quadrupole shift, ε is the quadrupole shift parameter, B_{hf} is the magnetic hyperfine field, and σ_{Δ} and $\sigma_{B_{hf}}$ are sigma-width of the QSD and HFD components. The $\chi_{Fe(II)}$ values were systematically higher in the samples melted at higher temperatures and agreed well with the spectrophotometrically determined $\chi_{Fe(II)}$ values [18]. Fe^{3+} doublet and sextet contributions to the spectra decreased slightly with a simultaneous increase in the Fe^{2+} doublet content. The small differences between the spectra are apparent from Fig. 3 where spectra of glasses melted at lowest and highest temperatures are compared.

The associated calculated Mössbauer parameters of the samples are summarized in Table 2, and they are defined as follows: $\langle CS \rangle$ is the average CS, $\langle QS \rangle$ is the average magnitude (i.e, average absolute value) of the QS, σ_{QSD} is the standard deviation from the average QS, $\langle \varepsilon \rangle$ is the average magnitude of the QS shift parameters (ε), $\langle B_{hf} \rangle$ is the average magnitude of the hyperfine field, and $\sigma_{B_{hf}}$ is the deviation from the average B_{hf}. In general, with heating, as expected, there were changes in the local chemical and structural environments of the samples, as was evident from both the calculated Mössbauer parameters (Table 2) and their QSD and HFD distributions (Fig. 8). The calculated Mössbauer parameters and QSD distribution of the Fe^{3+} environment of the 1300 °C sample were similar to those reported for Fe^{3+} in octahedral environment in Fe(III)-oxide systems [37,38]. With further increase in the melting temperature, there were subsequent changes in the Mössbauer parameters and QSD distributions. This was particularly evident in the Fe^{3+} doublet environment, both the $\langle QS \rangle$ and the QSD distribution widths decreased linearly with increase in temperature (Fig. 8(b)). The spread in QS occurs because of local changes in chemical and structural environment [27,28]. The QSD represents the most crystal chemical information that can be extracted from a spectrum [27,28]. These decreases in $\langle QS \rangle$ and QSD widths could be due to increase in tetrahedral character (or proportion) of the Fe^{3+} environment/sites. Rancourt et al. (1992) [39] and Rancourt et al. (2001) [37] showed that tetrahedrally coordinated Fe^{3+}

[2] Simulation of the 1400 °C sample was not carried out due to its poor signal-to-noise ratio.

Table 1
4.2 K Mössbauer fitting parameters and Fe^{2+}/Fe-total ratios of glasses melted at different temperatures

Melting temperature (°C)	Fe-sites	Mössbauer parameters					% Area	Fe^{2+}/Fe-total or $\chi_{Fe(II)}$	
		δ (mm/s)	Δ or ε (mm/s)	B_{hf} (T)	σ_Δ or $\sigma_{B_{hf}}$ (mm/s or T)	χ^2 (red)		Mössbauer	Spectrophotometry[a]
1300	Fe^{2+} doublet	1.12 (0.055)	2.5 (0.11)	–	0.54 (0.11)	1.10	6.8 (0.8)	0.068 (0.008)	0.062 (0.022)
	Fe^{3+} doublet	0.461 (0.032)	0.82 (0.05)	–	0.549 (0.049)		14.6 (0.7)		
	Fe^{3+} sextet	0.441 (0.014)	−0.062 (0.014)	–	–		78.6 (1)		
	Component 1			53.58 (0.12)	2.0[b]		21.1		
	Component 2			33.1 (1.2)	18.0[b]		57.5		
1500	Fe^{2+} doublet	1.115 (0.028)	2.36 (0.055)	–	0.52 (0.095)	0.9	13.7 (0.6)	0.137 (0.008)	0.144 (0.043)
	Fe^{3+} doublet	0.485 (0.037)	0.65 (0.06)	–	0.466 (0.049)		12.9 (1.4)		
	Fe^{3+} sextet	0.419 (0.024)	−0.058 (0.024)	–	–		73.5 (1.5)		
	Component 1			53.42 (0.22)	3.12 (0.29)		31.1		
	Component 2			28.5 (1.9)	14.3 (2.25)		42.3		
1600	Fe^{2+} doublet	1.124 (0.015)	2.35 (0.029)	–	0.55[b]	1.27	15.1 (1)	0.151 (0.01)	0.173 (0.023)
	Fe^{3+} doublet	0.395 (0.036)	0.62 (0.06)	–	0.408 (0.029)		10.9 (1)		
	Fe^{3+} sextet	0.437 (0.012)	−0.073 (0.012)	–	–		74.2 (1.5)		
	Component 1			53.55 (0.11)	2.51 (1.5)		27.8		
	Component 2			25.2 (1.95)	17.8 (1.95)		46.2		

[a] Jeoung et al. (2001).
[b] These parameters were fixed during the fitting process.

environments exhibit lower ⟨QS⟩ and smaller distribution widths than those of Fe^{3+} in octahedral environments. Rancourt et al. (1994) [39] and Coey 1980 [40] also showed that the tetrahedral Fe^{3+} ions have lower CS and QS values than those of octahedral Fe^{3+} environments.

Table 2
Calculated Mössbauer parameters of glasses melted at different temperatures

Melting temperature (°C)	Fe-site	⟨CS⟩ (mm/s)	⟨QS⟩ (mm/s)	σ_{QSD} (mm/s)	⟨ε⟩ (mm/s)	⟨B_{hf}⟩ (T)	σ_{HFD} (T)
1300	Fe^{2+} doublet	1.12	2.5	0.54	–	–	–
	Fe^{3+} doublet	0.46	0.85	0.5	–	–	–
	Fe^{3+} sextet	0.44	–	–	−0.062	38.95	17.15
1500	Fe^{2+} doublet	1.14	2.36	0.46	–	–	–
	Fe^{3+} doublet	0.48	0.71	0.45	–	–	–
	Fe^{3+} sextet	0.42	–	–	−0.058	39.22	16.18
1600	Fe^{2+} doublet	1.12	2.35	0.41	–	–	–
	Fe^{3+} doublet	0.39	0.69	0.46	–	–	–
	Fe^{3+} sextet	0.44	–	–	−0.073	36.63	18.22

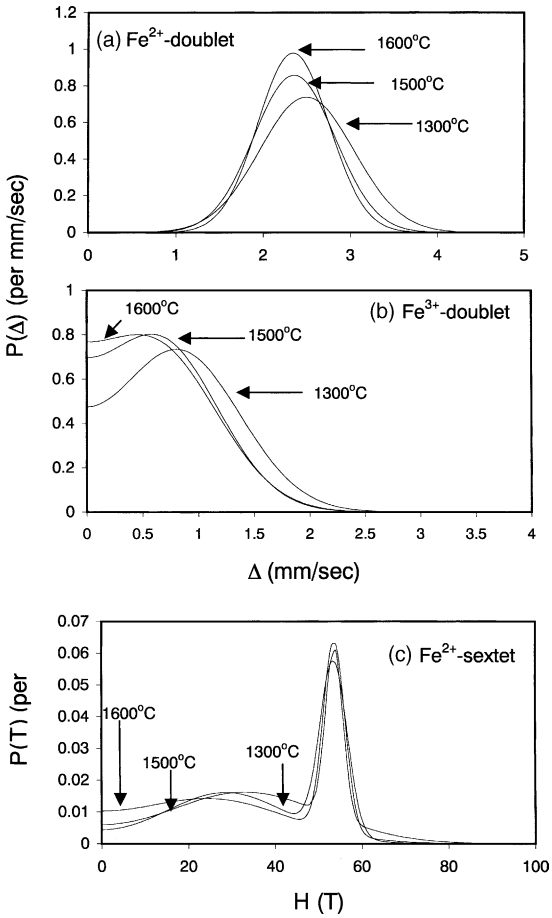

Fig. 8. QSD and HFD distributions of Fe-sites for the glasses melted in air at 1300, 1500 and 1600 °C.

The changes in the Fe^{2+} doublet and Fe^{3+} sextet features were less pronounced than the Fe^{3+} doublet (Fig. 8(a) and (c)). Both QS and distribution width of Fe^{2+} decreased with increase in melting temperature. These difference indicated changes in Fe^{2+} structural environment. The changes in Fe^{3+} sextet were more pronounced in the HFD distribution of the second Gaussian component of the spectra (wider distribution, 0–50 T region), particularly the width of the distribution. This indicated that this fraction of the Fe^{3+} sextet sites were relatively more susceptible to heat treatment than the Fe^{3+} sextet sites that comprise the first Gaussian component (sharp feature) of the distribution. A distribution of HFD in an annite clay was recently attributed to Fe(III)-oxides of varying crystallinity [37].

3.3.2. Samples prepared under reducing conditions

The reduction of ferric to ferrous irons was significant in the presence of CO/CO_2. For instance, at 1500 °C, the Mössbauer-derived $\chi_{Fe(II)}$ values for the glass melted in air and under $12CO/88CO_2$ were 0.137 and 0.277, respectively. At a constant temperature of 1500 °C, ferric to ferrous reduction proceeded further from 0.277 to 0.868 (based on Mössbauer data) under more reducing conditions from $12CO/88CO_2$ to $50CO/50CO_2$ (Table 3). The Mössbauer-derived $\chi_{Fe(II)}$ values agreed with the spectrophotometrically determined values (Table 3). The increase in $\chi_{Fe(II)}$ appeared mainly due to a systematic decrease in the Fe^{3+} sextet content. The Fe^{3+} sextet was not detectable in the highly reduced sample, the $50CO/50CO_2$ sample, and this may be due to its complete reduction to Fe^{2+}. The Fe^{3+} doublet content appeared to be stable towards the reducing atmosphere. Therefore, the Mössbauer fitting parameters of the Fe^{3+} doublet were constrained in all the reduced samples to values identical to that of the 1600 °C sample. In other words, an identical Fe^{3+} doublet environment was chosen to fit the spectra. This assumption seemed reasonable since the resultant fits yielded $\chi_{Fe(II)}$ values that were similar to the spectrophotometrically determined values.

The associated calculated Mössbauer parameters of the samples are summarized in Table 4. The parameters of Fe^{2+} doublet were similar in all the samples, except the $36CO/64CO_2$ reduced sample. The $36CO/64CO_2$ reduced sample also differed significantly from the others in its Fe^{3+} sextet parameters. The differences between the $36CO/64CO_2$ reduced sample and others were obvious from Fig. 5 (Mössbauer spectra) and Fig. 9. Fig. 9 compares QSD and HFD distributions of Fe^{2+} doublet and Fe^{3+} sextet of all the reduced samples. The differences in the Fe^{3+} sextet features between the samples ($12CO/88CO_2$, $24CO/76CO_2$, and $36CO/64CO_2$) was particularly evident in their $B_{hf(av)}$ values (Table 4), and HFD distribution of the second component (wider distribution) (Fig. 9). Samples reduced under $12CO/88CO_2$ and $24CO/76CO_2$ differed from each other mainly in

Table 3
4.2 K Mössbauer fitting parameters and Fe^{2+}/Fe-total ratios of glasses melted under CO and CO_2 gas mixture

CO:CO_2 ratio	Fe-sites	Mössbauer parameters					% Area	Fe^{2+}/Fe-total or $\chi_{Fe(II)}$	
		δ (mm/s)	Δ or ε (mm/s)	$B_{hf(av)}$ (T)	σ_Δ or $\sigma_{B_{hf}}$ (mm/s or T)	χ^2 (red)		Mössbauer	Spectrophotometry[a]
12:88	Fe^{2+} doublet	1.135 (0.009)	2.263 (0.018)	–	0.55[b]	1.25	27.7 (1.2)	0.277 (0.017)	0.360 (0.003)
	Fe^{3+} doublet	0.37[b]	0.62[b]		0.4[b]		7.9 (0.8)		
	Fe^{3+} sextet	0.426 (0.017)	−0.023 (0.017)	–	–		64.4 (1.48)		
	Component 1			53.59 (0.16)	2.37 (0.20)		20.7[b]		
	Component 2			31.7 (2.1)	18.3 (1.8)		43.7		
24:76	Fe^{2+} doublet	1.147 (0.001)	2.225 (0.016)	–	0.57[b]	0.99	48.2 (2.4)	0.482 (0.030)	0.515 (0.012)
	Fe^{3+} doublet	0.37[b]	0.62[b]	–	0.4[b]		9.2 (0.87)		
	Fe^{3+} sextet	0.429 (0.036)	0.07 (0.03)	–	–		42.6 (2.7)		
	Component 1			53.32 (0.34)	2.65 (0.50)		16.7		
	Component 2			40.1 (3.4)	11.4 (3.1)		26.0		
36:64	Fe^{2+} doublet	1.498 (0.12)	3.06 (0.02)	–	0.78 (0.02)	1.11	61 (0.9)	0.61 (0.0123)	0.612 (0.01)
	Fe^{3+} doublet	0.37[b]	0.62[b]	–	0.4[b]		7.6 (1)		
	Fe^{3+} sextet	0.481 (0.03)	0.09 (0.03)	70.8 (0.3)	3.36[b]		31.4 (0.61)		
50:50	Fe^{2+} doublet	1.14 (0.002)	2.235 (0.005)	–	0.542 (0.006)	2.21	86.85 (0.47)	0.878 (0.007)	0.908 (0.003)
	Fe^{3+} doublet	0.37[b]	0.62[b]	–	0.4[b]		13.15 (0.47)		

[a] Jeoung et al. (2001).
[b] Fixed parameter.

Table 4
Calculated Mössbauer parameters of glasses melted under CO and CO_2 gas mixture

Melting temperature (°C)	Fe-site	$\langle CS \rangle$ (mm/s)	$\langle QS \rangle$ (mm/s)	σ_{QSD} (mm/s)	$\langle \varepsilon \rangle$ (mm/s)	$\langle B_{hf} \rangle$ (T)	σ_{HFD} (T)
12:88	Fe^{2+} doublet	1.13	2.26	0.55	–	–	–
	Fe^{3+} doublet	0.37	0.64	0.37	–	–	–
	Fe^{3+} sextet	0.43	–	–	−0.022	39.21	17.42
24:76	Fe^{2+} doublet	1.15	2.22	0.57	–	–	–
	Fe^{3+} doublet	0.39	0.64	0.37	–	–	–
	Fe^{3+} sextet	0.43	–	–	0.07	45.28	11.13
36:64	Fe^{2+} doublet	1.5	3.05	0.8	–	–	–
	Fe^{3+} doublet	0.37	0.64	0.37	–	–	–
	Fe^{3+} sextet	0.48	–	–	0.09	70.81	3.36
50:50	Fe^{2+} doublet	1.15	2.23	0.54	–	–	–
	Fe^{3+} doublet	0.37	0.64	0.37	–	–	–

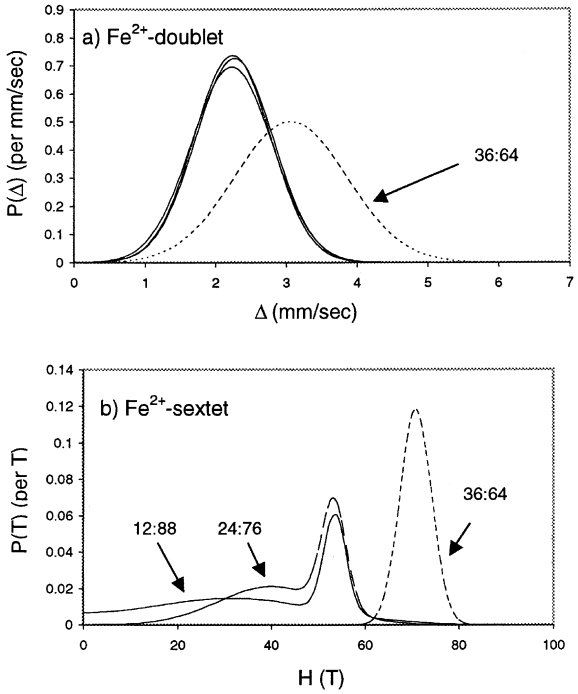

Fig. 9. QSD and HFD distributions of Fe-sites for the glasses melted for the glasses melted in CO/CO_2 atmosphere (12/88 to 50/50).

the σ_{HFD} of the second component (Fig. 9). This implied that Fe^{3+} sites that contribute to the second component were more susceptible to the reduction, a finding similar to that of the temperature effect. The σ_{HFD}, however, was simpler for the $36CO/64CO_2$ sample; a single component was sufficient to fit its sextet pattern. For the $50CO/50CO_2$ sample, the sextet feature disappeared completely (cf. Fig. 5). These changes in the Fe^{3+} sextet appeared to be related to the changes in the 375-nm optical band (Fig. 1(e)).

4. Discussion

4.1. Mössbauer-derived iron redox

The liquid-helium Mössbauer-derived $\chi_{Fe(II)}$ values of all the glasses studied agree, within the uncertainties of measurements and simulations, with those determined by optical methods (Tables 1 and 3). The observation was in agreement with the recent study of silicate glasses containing <4 mol% Fe_2O_3 by Bingham et al. [35] where the Mössbauer-derived $\chi_{Fe(II)}$ values (based on a Lorentzian fit model) were identical to those calculated by an optical method. The Mössbauer-derived $\chi_{Fe(II)}$ values from fitting RT spectra (except for the highly reduced sample, the $50CO/50CO_2$ sample), however, were consistently higher than those derived from the 4.2 K spectra (data not shown). In a soda-lime silicate with less than 0.5 wt% Fe_2O_3, Williams et al. [41,42] observed differences between the RT Mössbauer spectroscopy-derived $\chi_{Fe(II)}$ values and other techniques. This implied that the iron redox of glasses with low iron content cannot be accurately determined using the RT spectra. In our study, the $\chi_{Fe(II)}$ results derived from RT and 4.2 K were close to each other only for the highly reduced sample, the sample with no detectable curved baseline at RT.

4.2. General ^{57}Fe Mössbauer features

Two types of Fe^{3+} environments, a magnetic Fe^{3+} sextet(s) and a paramagnetic Fe^{3+} doublet, were evident in the 4.2 K Mössbauer spectra of most of the samples. The sextet is referred to as a paramagnetic HFS and arises due to the lack or decreased spin–spin interaction between Fe^{3+} sites at lower iron contents. [3] Decreased Fe concentration (increased Fe–Fe separation) increases the spin–spin relaxation time [43]. The observation of HFS spectra in kaolinite samples with low Fe content was ascribed to HFS [36]. As the Fe content increases, the probability of spin–spin interaction increases between the adjacent sites, causing the HFS peaks to be transferred to a doublet. In the samples under current investigation, the sextet

[3] Unlike in the Fe^{3+} ions, only a Fe^{2+} doublet feature was evident in the spectra, regardless of the $\chi_{Fe(II)}$ of samples. The sextet feature due to the Fe^{2+} environment was not evident in any sample. This was expected because the spin–spin relaxation rate of the Fe^{2+} ions was faster than that exhibited by the Fe^{3+} ions; the rate was higher because of the coupling of the lattice modes to the total angular momentum via the orbital contribution.

feature likely represents isolated Fe^{3+} ions rather than an ordered magnetic phase; e.g., magnetite. No secondary phases (crystalline or amorphous) were detectable using transmission electron microscopy in these samples.

4.3. Melting temperature effect on iron local environments

The optical peaks due to Fe^{3+} (350–500 nm) were identical in all the melted samples, based on Fig. 1(c), irrespective of the $\chi_{Fe(II)}$ of the sample, implying that (1) identical Fe^{3+} environments existed in all the melted samples and (2) both the doublet and sextet Fe^{3+} environments were reduced proportionately. Small changes in the Fe^{3+} features, particularly for Fe^{3+} doublet, however, were apparent in their Mössbauer QSD and HFD distributions (Fig. 8).

The slightly lower $\langle CS \rangle$ and $\langle QS \rangle$ of the Fe^{3+} doublet in the 1600 °C (Table 2) sample compared to other melted samples may suggest a slightly different coordination environment than the others. Its parameters, based on a fit of the data, were similar to the derived values for tetrahedral Fe^{3+} ions ($\langle CS \rangle = 0.39$ mm/s and $\langle QS \rangle = 0.62$ mm/s) [44]. Its contribution to the spectrum was identical to that of the Fe^{3+} doublet contribution in the reduced samples, approx. 10% (Tables 1 and 3), but was lower than the other air-melted samples (1300–1500 °C samples); e.g., the Fe^{3+} doublet contribution was 15% in the 1300 °C sample. The differences in Fe^{3+} doublet content between the samples indicate that some fraction of the Fe^{3+} doublet in the 1300–1500 °C range was thermally unstable and may have had different chemical and structural environments from the 1600 °C sample. However, since the spectral features were not resolved into two doublets in these samples, it was not physically meaningful to fit the feature into two doublets to extract their parameters.

Similar Fe^{3+} sextet features, a curved baseline and a broad sextet feature with no apparent resolution into multiple sextets, were evident in all the samples. If there was any change between the Fe^{3+} sextet features, the variation must have been small and confined to changes in the distribution of local environments. HFD models were routinely employed to fit Mössbauer spectra to account for the distribution of Fe^{3+} environments [45]. Because of lack of evidence for multiple sextets in our samples, we fitted the sextet feature with one sextet that has two Gaussian components (Components 1 and 2) along with the HFD model. Fit data clearly indicated that these Fe^{3+} environments of the melted samples were slightly different from each other; they vary mainly in their $B_{h(av)}$ and σ_{HFD} of the second component (Fig. 8(c)). To our knowledge, the nature of the sextet feature was not addressed adequately in the literature. Bingham et al. [35] recently fitted Mössbauer spectra of sodium silicate glasses with two sextets without any physical assignments. We argue that these Fe^{3+} sites represented by the sextet have an octahedral environment (discussed in Section 4.4).

Like the Fe^{3+} sites, the Fe^{2+} environment was stable towards the melting temperature. This was evident from their optical spectra (Fig. 1(b)) and Mössbauer parameters (Table 2 and Fig. 8); the optical bands and Mössbauer parameters were essentially identical for all the samples. The coordination nature (tetrahedral or octahedral) of Fe^{2+}, however, was not straightforward. The two broad Fe^{2+} peaks at 1120 and 2020 nm in the optical spectra were assigned in the literature differently. Steele and Douglas [31], based on ligand field predictions, assigned the 1120-nm peak to octahedral Fe^{2+} and the 2020-nm peak to tetrahedral Fe^{2+} ions. The assignment of the 2020 band to tetrahedral Fe^{2+}, however, has been controversial; some supported tetrahedral configuration [46–49] whereas Edwards et al. [50] interpreted it to be in a distorted octahedral coordination.

The calculated Mössbauer parameters, on the other hand, were typical of Fe^{2+} in an octahedral environment. Bingham et al. [35] reported similar $\langle CS \rangle$ and $\langle QS \rangle$ for octahedral Fe^{2+} in SiO_2-Na_2O-CaO glass containing ~1% Fe_2O_3. Furthermore, the Fe^{2+} doublet feature in our glasses lacks features that imply the presence of more than one Fe^{2+} doublet or environments, Fe^{2+}_{oct} and Fe^{2+}_{tet}, in contrast to the results in the literature [46–49]. This and the near constant ratio of the 1120- and 2020-nm optical bands in all the samples indicated that these bands were probably due to octahedral Fe^{3+} coordinations with different distortions rather

than Fe^{2+} in octahedral and tetrahedral coordinations.

4.4. Effect of CO/CO_2 atmosphere on iron environments

Unlike in the air-melted sample, the reducing atmosphere had a pronounced effect on the Fe^{3+} sextet features. Its intensity varied significantly with simultaneous changes in Mössbauer parameters, particularly between the $12CO/88CO_2$ and $24CO/76CO_2$, and $36CO/64CO_2$ samples, with an increase in the CO/CO_2 ratio. The Fe^{3+} doublet's Mössbauer parameters (Table 4) and intensity (Table 3), on the other hand, were not affected significantly. Its intensity and parameters were identical to that of the stable tetrahedral Fe^{3+} sites identified in the 1600 °C air-melted sample. Identical Mössbauer parameters among the various reduced samples were further indicative of the stability of these ions.

The parameters of the Fe^{3+} sextet for the $12CO/88CO_2$ and $24CO/76CO_2$ samples were similar, which were also similar to the parameters of air-melted samples. However, the sextet feature of the $36CO/64CO_2$ sample was significantly different than the former reduced samples. Specifically, its derived $B_{hf(av)}$ value of 70.8 T was much higher than approximately 53 T for the $12CO/88CO_2$ and $24CO/76CO_2$ samples as well for the samples melted under ambient conditions. The result, an HFS spectrum with such a high $B_{hf(av)}$ value, is unusual. Further investigation is necessary, examining whether it is related to decreased spin–spin interactions of the Fe^{3+} ions. In Na_2O_3–$3SiO_2$ glasses with varying Fe_2O_3 content (0.1–1 mol%), a 0.1 mol% Fe_2O_3 glass exhibited ~10% higher apparent B_{hf} value than that of a 1 mol% Fe_2O_3 glass (Fig. 8 in Ref. [33]; note: the x-axis scale varies for the spectra). A decrease in the sextet content implies that the majority of isolated Fe^{3+} ions were converted to Fe^{2+} ions. The trend in the conversion of Fe^{3+} to Fe^{2+} ions was further evident from the absence of a sextet feature in the most reduced $50CO/50CO_2$ sample.

The significant changes in Mössbauer and optical spectra with the CO/CO_2 ratio, unlike in the air-melted samples, helped to interpret the optical bands and their relation to Mössbauer peaks. For example, the 375-nm band was assigned to both the octahedral Fe^{3+} and tetrahedral Fe^{3+} transitions $[^6\Gamma_1–^4\Gamma_5(D)]$ [32]. The position is the same compared to our results. Both the 375-nm optical band and the Fe^{3+} sextet Mössbauer intensities were progressively and simultaneously reduced. Therefore, it is likely that the 375 nm and Fe^{3+} sextet represent the same Fe^{3+} environment, and we assigned them to octahedrally coordinated irons for the following two reasons. First, the reduction of octahedral Fe^{3+} to tetrahedral Fe^{2+} is energetically unfavorable because the process involves an electron transfer from cation to oxygen without changing its coordination with oxygen. Secondly, the shift in the local electron density of the bonding environment between iron cation and oxygen are favored between iron cation and non-bridging oxygen over bridging oxygen.

The absorption band near 415 nm obtained from our study is close to the 427-nm band, based on a theoretical calculation for the $^6\Gamma_1–^4\Gamma_1$, $^4\Gamma_3(G)$ transition of tetrahedral Fe^{3+} ions and octahedral Fe^{3+} ions [32]. The $^6\Gamma_1–^4\Gamma_5(G)$ transition of tetrahedral Fe^{3+} ions was predicted at 500 nm [32] as compared to a small broad band near 485 nm from our study. For octahedral Fe^{3+} ions, the predicted transition of $^6\Gamma_1–^4\Gamma_5(G)$ was at 570 nm, but at 446 nm for tetrahedral Fe^{3+} ions [32]. In our study, a band at 435 nm was observed. The above bands obtained from our study showed little change over the wide temperature and melt redox conditions (cf. Fig. 1(c) and (f)). Combining the Mössbauer fitting results with the observed optical band characteristics and the literature predictions, we propose that the optical bands near 415, 435, and 485 nm likely relate to the tetrahedral coordinated ferric ions as represented by the Fe^{3+} doublet (cf. Mössbauer data, Section 4.3).

Like the Fe^{3+} sextet parameters, the Fe^{2+} doublet parameters of the $36CO/64CO_2$ sample differed significantly from the mildly reduced and air-melted samples; its $\langle CS \rangle$ and $\langle QS \rangle$ values were significantly higher. Such high $\langle CS \rangle$ (1.5 mm/s vs. ~1.16 mm/s for the other samples) and $\langle QS \rangle$ values (3.06 mm/s vs. ~2.20 mm/s for the other samples) for a Fe^{2+} doublet have been reported by

Boon [51] for an Fe-rich silicate glass and by Kamo et al. [52] for a phosphate glass ($Fe_3O_4 \cdot NaPO_3$). In general, an increase in ⟨CS⟩, opposite to the case of Fe^{3+} environment, indicates an increase in symmetry or decrease in distortion around the Fe^{2+} ion. Labar and Gielen [53] attributed an increase in ⟨QS⟩ to a change in coordination to an increasingly octahedral coordination. An increase in ⟨CS⟩was also attributed to a change in coordination towards an increasingly octahedral coordination [50]. The differences in Fe^{2+} features between the $36CO/64CO_2$ and other reduced samples, however, were not apparent in the optical spectra (Fig. 1(a)); spectral features of the bands at 1120 and 2020 nm were similar in all the samples.

The asymmetry of the doublet feature in the Mössbauer spectrum of the highly reduced sample ($50CO/50CO_2$ sample; Fig. 5(d)) is not due to the Goldanskii effect as hypothesized by Kurkjian and Buchanan (Fig. 9 in Ref. [33]); Goldanskii has shown that in crystals, regardless of the anisotropy of the crystals, asymmetry results because of the anisotropy of the recoil-free fraction [54]. The asymmetry was a result of the presence of Fe^{2+} and Fe^{3+} environments (Table 3), as obvious from $\chi_{Fe(II)}$ and the optical data.

4.5. Assignment of Fe-sites

The results discussed so far support the coexistence of Fe^{3+}_{tet}, Fe^{3+}_{oct}, and Fe^{2+}_{oct} environments in the glass samples. Specifically, the Fe^{3+} sextet represents isolated octahedral ferric ions (with a wide distribution), and this feature is related to the 375-nm optical band. The feature is not due to a Fe-oxide phase, e.g., inverse spinel-like magnetite. The Fe^{3+} doublet primarily represents tetrahedral ferric ions, which is related to 415-, 435-, and 485-nm optical bands. Finally, the Fe^{2+} doublet represents octahedral ferrous ions with varying distortions, which is related to the optical bands near 1120 and 2020 nm. It was also evident from the study that ~10% of Fe^{3+} exists in tetrahedral coordination in all the samples, a fraction that appears to be stable over the changes of melting temperature and oxygen partial pressure. The increase in the Fe^{2+}_{oct} content in the reduced samples appears solely due to the reduction of the Fe^{3+}_{oct} ions.

4.6. Effect of iron doping and oxidation state on immiscibility

On the one hand, as previously reported, 0.5 mol% Fe_2O_3 doping significantly decreased T_c by 32 and 29 °C for 18NS and 13NS glasses, respectively, when the melts were prepared at different temperatures in ambient conditions [18]. On the other hand, a change in the ferrous and ferric ion ratio was shown to have a secondary effect on T_c, by less than 5 °C, for the iron-doped glasses [18]. Based on the above study, we propose two possible roles for ferrous and ferric ions on phase separation in the system under investigation. First, Fe^{3+}_{tet} ions, about 10% of the total iron, function as a glass network former that is expected to decrease the tendency of glass phase separation, possibly by forming bonding with Na similar to the effect of Al on depressing the immiscibility of sodium silicate glass [55]. Secondly, the Fe^{3+}_{oct} and/or Fe^{2+}_{oct} ions may function as a network modifier. Hence, one would also expect a decrease in T_c as total iron increases since the composition of 18NS is within the immiscibility dome and at the right side of the dome [55]. Finally, the small effect of Fe^{2+}_{oct} on increasing T_c may further suggest that Fe^{2+}_{oct} behaved more like divalent alkaline earth cations that are known to increase T_c.

5. Conclusions

Local iron environments of ferric and ferrous were systematically studied using Mössbauer (at liquid helium temperatures) and UV–VIS–NIR spectroscopic methods. These environments existed in a single iron-doped sodium silicate glass heated to 1300–1500 °C under air or heated at 1500 °C under varying CO/CO_2 ratios (12/88 to 50/50). The oxidation-reduction (or $\chi_{Fe(II)}$) was controlled by both temperature and an oxidization state of the melt. Reducing atmosphere (CO/CO_2) had a significant effect on $\chi_{Fe(II)}$. For the current system, we identified limited tetrahedral sites for ferric ions, Fe^{3+}_{tet}, that are stable against reduction

to ferrous ions even under the most reducing condition, 50CO/50CO_2, applied. The majority of ferric ions likely occupy the octahedral sites, Fe^{3+}_{oct}, that were isolated and were readily converted into ferrous ions, Fe^{2+}_{oct}, without changing its coordination. Combining results from both spectroscopic studies, the 1120- and 2020-nm optical bands were linked to Fe^{2+}_{oct} ions with a different degree of distortion rather than different coordinations. Further, we assigned a 375-nm band to the transition of octahedral ferric ions, Fe^{3+}_{oct}, which is sensitive to the change of oxygen partial pressure in glass melting and 415-, 435-, and 485-nm bands to the transitions of the tetrahedral ferric ions, Fe^{3+}_{tet}, which are insensitive to oxidation states of the melt. Based on the spectroscopy-derived local iron environments from this study and our previous work, the effect of ferric and ferrous ions with different coordination environments on the glass immiscibility was discussed within a contest of different structural roles between Fe^{3+}_{tet} as network former suppressing immiscibility and Fe^{2+}_{oct} and/or Fe^{3+}_{oct} as network modifiers or intermediate, either suppressing or increasing immiscibility slightly at the current concentration level.

The use of both techniques enables us to better identify specific local environments of iron species under various melting conditions. However, the overall results point out the complexity of the iron effects on silicate phase separation. For complex borosilicate glasses currently developed for immobilizing radioactive materials, the effects of ferrous and ferric ions are expected to be more complicated because of the coexistence of two network-forming structures, Si–O and B–O, and partitioning of these iron species between the two network environments. This is strongly affected by other major constituents, such as Al and Na. Further studies of such a complex system are highly recommended, which is very important for long-term safe storage of radioactive waste materials.

Acknowledgements

This work is funded by the US Department of Energy through the Environmental Management Science Program. Pacific Northwest National Laboratory is operated by Battelle for the US Department of Energy under Contract DE-AC06-76RL01830. Mössbauer measurements were performed within the DOE/Office of Biological and Environmental Research (OBER) Environmental Molecular Sciences Laboratory (EMSL) user facility.

References

[1] W. Lutz, in: W. Lutz, R.C. Ewing (Eds.), Radioactive Waste Forms for the Future, North-Holland, New York, 1988, p. 1 (Chapter 1).
[2] L.L. Hench, R.J. Charles, A.R. Cooper, R.C. Ewing, J.R. Hutchins, D.W. Readey, F.L. VerSnyder, S.M. Widerhorn, The Evaluation and Selection of Candidate High Level Waste Forms: Report no. 1 USDOE/TIC-10228 (1979), Report no. 2 USDOE/TIC-11219 (1980), and Report no. 3 USDOE/TIC-11472 (1981), Alternative Form Peer Review Panel, National Technical Information Service, Springfield, VA.
[3] P.R. Hrma, G.F. Piepel, M.J. Schweiger, D.E. Smith, D.-S. Kim, P.E. Redgate, J.D. Vienna, C.A. LoPresti, D.B. Simpson, D.K. Peeler, M.H. Langowski, Property/Composition Relationships for Hanford High-Level Waste Glasses Melting at 1150 °C, Report PNL-10359, vol. 1, 2, UC-721, Pacific Northwest National Laboratory, Richland, WA, December 1994.
[4] D.S. Goldman, D.W. Brite, J. Am. Ceram. Soc. 69 (1986) 411.
[5] D.S. Goldman, J. Am. Ceram. Soc. 66 (1983) 205.
[6] H.D. Schreiber, S.J. Kozak, B.D. Trandel, C.W. Schreiber, in: D.E. Clark, W.B. White, A.J. Machiels (Eds.), Advances in Ceramics, vol. 20, American Ceramic Society, Westerville, OH, 1986, p. 125.
[7] H.D. Schreiber, C.W. Schreiber, C.C. Ward, in: C.G. Interrante, R.T. Pabalan (Eds.), Scientific Basis for Nuclear Waste Management XVI, vol. 294, MRS, Pittsburgh, PA, 1983, p. 87.
[8] C.M. Jantzen, D.F. Bickford, in: C.M. Jantzen, J.A. Stone, R.C. Ewing (Eds.), Scientific Basis for Nuclear Waste Management VIII, vol. 44, Materials Research Society, Pittsburgh, PA, 1985, p. 135.
[9] P. Hrma, Ceram. Trans. 45 (1994) 391.
[10] D.S. Kim, P. Hrma, Ceram. Trans. 45 (1994) 327.
[11] P. Hrma, J.D. Vienna, M.J. Schweiger, Ceram. Trans. 72 (1996) 449.
[12] P. Hrma, J.D. Vienna, J.V. Crum, G.F. Piepel, in: Scientific Basis for Nuclear Waste Management XXIII 608 (2000) p. 671.
[13] M. Mika, M.J. Schweiger, J.D. Vienna, P. Hrma, Scientific Basis for Nuclear Waste Management XX 465 (1997) 71.

[14] P. Hrma, P. Izak, J.D. Vienna, M.L. Thomas, G.M. Irwin, Phys. Chem. Glasses 43 (2002) 119.
[15] D.K. Peeler, P.R. Hrma, Ceram. Trans. 45 (1994) 219.
[16] P. Taylor, A Review of Phase Separation in Borosilicate Glasses with Reference to Nuclear Fuel Waste Immobilization, Report AECL-10173, Atomic Energy of Canada Limited, RECL Research Whileshell Laboratories, Pinawa, Manitoba, Canada, 1990.
[17] M. Tomozawa, G.M. Singer, R.K. MacCrone, J.T. Warden, J. Non-Cryst. Solids 49 (1982) 165.
[18] J.S. Jeoung, W.H. Poisl, M.C. Weinberg, G.L. Smith, H. Li, J. Am. Ceram. Soc. 18 (2001) 1859.
[19] W.J. Dell, P.J. Bray, S.Z. Xiao, J. Non-Cryst. Solids 20 (1976) 192.
[20] Y.H. Yun, P.J. Bray, J. Non-Cryst. Solids 27 (1978) 363.
[21] K. Garterer, in: A.C. Wright, S.A. Feller, A.C. Hannon (Eds.), Borate Glasses, Crystals and Melts, Society of Glass Technology, Sheffield, 1997, p. 384.
[22] S. Wang, J.F. Stebbins, J. Am. Ceram. Soc. 82 (1999) 1519.
[23] H. Li, L. Li, J.D. Vienna, M. Qian, Z. Wang, J.G. Darab, D.K. Peeler, J. Non-Cryst. Solids 278 (2000) 35.
[24] C.W. Bale, FACT-Win, Thermochemical Database, CRCT, École Polytechnique de Montréal, Canada, 1976.
[25] D.G. Rancourt, J.Y. Ping, Nucl. Instrum. Meth. 58 (1991) 85.
[26] V.F. Weisskoff, E. Wigner, Z. Phys. 63 (1930) 54.
[27] D.G. Rancourt, Phys. Chem. Mineral. 21 (1994) 244.
[28] D.G. Rancourt, Phys. Chem. Mineral. 21 (1994) 250.
[29] D.G. Rancourt, J.Y. Ping, R.G. Berman, Phys. Chem. Mineral. 21 (1994) 258.
[30] S. Rossano, E. Balan, G. Morin, J.-P. Bauer, G. Calas, C. Brouder, Phys. Chem. Mineral. 26 (1999) 530.
[31] F.N. Steele, R.W. Douglas, Phys. Chem. Glasses 6. (1965) 246.
[32] N.N. Greenwood, T.C. Gibb, Mössbauer Spectroscopy, Chapman and Hall, London, 1971, p. 659.
[33] C.R. Kurkjian, D.N.E. Buchanan, Phys. Chem. Glasses 5 (1964) 63.
[34] G. Tomandl, Glass Sci. Technol. 48 (1990) 273.
[35] P.A. Bingham, J.M. Parker, T. Searle, J.M. Williams, K. Fyles, J. Non-Cryst. Solids 253 (1999) 203.
[36] S.A. Fysh, J.D. Cashion, P.E. Clark, Clays Clay Miner. 31 (1983) 285.
[37] D.G. Rancourt, D. Fortin, T. Pichler, P.-J. Thibault, G. Lamarche, R.V. Morris, P.H.J. Mercier, Am. Miner. 86 (2001) 834.
[38] R.K. Kukkadapu, J.M. Zachara, J.K. Fredrickson, A.C. Dohnalkova, S.C. Smith, C.K. Russell, Geochim. Cosmochim. Acta, submitted for publication.
[39] D.G. Rancourt, M.-Z. Dang, A.E. Lalonde, Phy. Chem. Miners. 21 (1994) 258.
[40] J.M.D. Coey, Atomic Energy Rev. 18 (1980) 73.
[41] K.F.E. Williams, M.F. Thomas, C.E. Johnson, B.P. Tilley, J. Greengrass, J.A. Johnson, in: Proc. Fundamentals of Glass Sci. Tech., 1997, p. 127.
[42] K.F.E. Williams, C.E. Johnson, M.F. Thomas, J. Non-Cryst. Solids 226 (1998) 19.
[43] J.W.G. Wignall, J. Chem. Phys. 44 (1966) 2462.
[44] M.D. Dyar, Am. Mineral. 70 (1985) 304.
[45] M.-Z. Dang, D.G. Rancourt, J.E. Dutrizac, G. Lamarche, R. Provencher, Hyperfine Interact. 117 (1998) 271.
[46] A.M. Bishay, L. Makar, J. Am. Ceram. Soc. 52 (1969) 605.
[47] A. Montenero, M. Friggeri, D.C. Giori, N. Belkhiria, L.D. Pye, J. Non-Cryst. Solids 84 (1986) 45.
[48] M. Ookawa, T. Sakurai, S. Mogi, T. Yokokawa, Mater. Trans. JIM 38 (1977) 220.
[49] C. Ades, T. Toganidis, J.P. Traverse, J. Non-Cryst. Solids 125 (1990) 272.
[50] R.J. Edwards, A. Paul, R.W. Douglas, Phys. Chem. Glasses 13 (1972) 137.
[51] J.A. Boon, Chem. Geol. 7 (1971) 153.
[52] M. Kamo, Y. Takashima, S. Ohashi, Bull. Chem. Soc. Jpn. 40 (1967) 2812.
[53] C. Labar, P. Gielen, J. Non-Cryst. Solids 13 (1973) 107.
[54] V.I. Goldanskii, E.F. Makarov, V.V. Khrapov, Phys. Lett. 3 (1963) 344.
[55] M. Tomozawa, R.A. Ohara, J. Am. Ceram. Soc. 56 (1973) 378.